Physica E 123 (2020) 114162

Contents lists available at ScienceDirect

Physica E: Low-dimensional Systems and Nanostructures

journal homepage: http://www.elsevier.com/locate/physe

Structural characterization of 3d metal adsorbed AgNPs

Irene Schiesaro [a,**], Chiara Battocchio [a], Iole Venditti [a], Paolo Prosposito [b], Luca Burratti [b], Paolo Centomo [c], Carlo Meneghini [a]

[a] Department of Sciences, Roma Tre University of Rome, Via della Vasca Navale 84, 00146, Rome, Italy
[b] Department of Industrial Engineering and INSTM, University of Rome Tor Vergata, via del Politecnico 1, 00133, Rome, Italy
[c] Department of Chemical Sciences, University of Padova, via Marzolo 1, I-35131, Padova, Italy

ARTICLE INFO

Keywords:
Silver nanoparticles
XAFS
Coordination chemistry
Co oxyhydroxides
Ni hydroxides

ABSTRACT

Silver nanoparticles AgNPs having small (6–8 nm) diameter, were synthesized in water in solutions and left interacting with diluted 3d metals (Co^{2+} or Ni^{2+} ions) solution (1–5 ppm range). The interactions between AgNPs and the metallic ions modify the optical response of the nanoparticles demonstrating their ability to capture metallic ions from water and making them valuable as metal contamination sensor. Here the coordination chemistry of Co and Ni adsorbed onto AgNPs is probed combining X-ray absorption spectroscopy (XAS) and X-ray photoelectron spectroscopy (XPS).

1. Introduction

The detection of heavy metal trace ions in liquid solutions has become a major challenge in research due to the negative impacts that these toxic elements can have on the environment and on human health [1–4]. Great attention is being paid to strategies suited for in-situ and/or rapid screening, being also easy and quick to use. In this context silver nanoparticles (AgNPs) promise to have a valuable role. The success of AgNPs in several fields ranging, to give a few examples, from sensors, catalysis, optoelectronic or environmental sciences [5–9], is mostly due to advantages such as their easy synthesis at low costs and the possibility to be functionalized in order to provide selective response to specific analytes.

The surface plasmon resonance (SPR), a phenomenon due to the resonant interaction of light with the conduction electrons of the nanoparticles [10], leads to a peak in the optical absorption, being related in a controlled and reproducible way to the particle dimension and morphology. In AgNPs the shape and energy of the SPR are modified by the NP chemical environment making the AgNPs suitable as sensitive and selective chemical sensors.

Previous studies [11,12] have been successful in the fabrication and characterization of optimized AgNPs as optical sensors for Ni^{2+} and Co^{2+}. Dynamic light scattering (DLS), Fourier Transform Infrared Spectroscopy (FTIR) and high resolution X-ray photoelectron (HR-XPS) spectroscopies revealed the formation of coordination compounds of AgNPs with the metal ions as the reason for their optical response. Furthermore AgNPs have been recently proposed as the core of functionalized nanomaterial able to selectively capture metallic ions from water in an aggregation phenomena process [13].

The aim of this work is to provide detailed chemical and structural characterization of AgNPs-Ni^{2+} and AgNPs-Co^{2+} coordination compounds looking at the electronic state and local atomic structure of Ag and Ni^{2+} and Co^{2+} exploiting the complementary information obtained by combining high resolution X-ray photoelectron spectroscopy (HR-XPS) and X-ray absorption fine structure (XAFS) techniques. From XPS measurements we assess the molecular stability and the electronic structure of the metal ions while the analysis of Ag, Ni and Co K-edge XAFS data in the near edge (XANES) and extended (EXAFS) spectral regions provides information about the oxidation state, local atomic structure and coordination chemistry around the absorbers.

2. Synthesis of 3MPS stabilized AgNPs

Deionized water (electrical conductivity less than 1 μΩ/cm at room temperature) obtained from a Millipore Milli-Q water purification system was used for the preparation of the aqueous solutions. All of the reagents were purchased from Sigma Aldrich and were used without further purification.

AgNPs stabilized with sodium 3-mercapto-1-propanesulfonate (3MPS) were synthesized starting with a volume of 700 ml of sodium borohydride water solution [$NaBH_4$] = 0.1513 mg/ml at T = 3 °C under vigorous stirring. 10 ml of this solution were used to solubilize 0.2 g of

* Corresponding author.
E-mail address: irene.schiesaro@uniroma3.it (I. Schiesaro).

https://doi.org/10.1016/j.physe.2020.114162
Received 28 February 2020; Received in revised form 18 April 2020; Accepted 24 April 2020
Available online 4 May 2020

3MPS (capping agent solution). A volume of 46 ml of $AgNO_3$ water solution [$AgNO_3$] = 0.342 mg/ml was added dropwise to the remaining solution (690 ml) while a small volume of the capping agent solution (84.3 μl) was introduced at the end of the synthesis [12]. The Ni^{2+} or Co^{2+} water solutions were prepared using $NiCl_2 \cdot 6H_2O$ and $CoCl_2 \cdot 6H_2O$.

The optical absorption measurements were aimed at verify the sensitivity of AgNPs to metal ions (Ni^{2+} or Co^{2+}) interactions. Samples for optical absorption were prepared adding 1 ml of the AgNP solution to 1 ml of water solution with 1 or 5 ppm of Ni^{2+} or Co^{2+} pollutants. After 5 min under continuous stirring to allow the complete mixing between heavy metal ions and silver nanoparticles, the AgNPs absorbance was measured.

The optical absorption spectra were collected in the range 300–700 nm (UV–Vis) using a PerkinElmer spectrophotometer (Lamba19 UV/Vis/NIR) on AgNPs and Co/Ni-AgNPs, the corresponding spectra are reported in Fig. 1. The absorption spectrum of bare AgNPs has a localized surface plasmon resonance with a sharper well defined maximum close to 400 nm which was taken as reference. The Fig. 1 shows the optical behaviour of AgNPs in the presence of 1 ppm and 5 ppm Co^{2+} ions. In 1 ppm Co^{2+} solution (red curve) a red shift from 400 nm (black line, reference) to 430 nm, associated to a decrease of the intensity and a broadening of the band, was observed. By increasing the Co^{2+} concentration up to 5 ppm, a similar effect on the absorbance (energy shift = 420 nm, and broadening of the band) is also accompanied by a significant increase of the light scattering (as suggested by the spectral background): this suggests the formation of larger aggregates at higher Co^{2+} concentration.

3. Experimental section

For XAS and XPS characterization, dry powders of AgNPs-Ni/Co were prepared from 2.8 l AgNPs solutions, obtained by adding 1.4 l of Ni^{2+} or Co^{2+} aqueous solutions (1 or 5 ppm; by using $NiCl_2 \cdot 6H_2O$ and $CoCl_2 \cdot 6H_2O$, respectively) to 1.4 l (2 × 700 ml) of AgNPs solution (see above). Solutions were dried in thermostated oven at T = 50 °C under continuous gentle stirring and dry powders were used for HR-XPS and XAFS analysis.

To prevent the degradation of the sample, the dry powders of bare (AgNPs) and metal loaded (M-# ppm -AgNPs) nanoparticles were stored under vacuum at room temperature until measurements. In the following the AgNPs solutions containing 1 ppm and 5 ppm of cobalt or nickel ions will be labelled as M-# ppm-AgNPs, with M = Co or Ni and # = 1 or 5).

X-ray absorption experiments were performed at the XAFS beamline of the ELETTRA synchrotron (Trieste, Italy) [14]. The absorption spectra were collected in transmission geometry at room temperature at the K edges of Co (E_{Co} = 7709 eV), Ni (E_{Ni} = 8331 eV) and Ag (E_{Ag} = 25514 eV). Samples were prepared mixing the fine sample powders with cellulose matrix (approximately 1:3 wt ratio) and pressing the mixture in form of solid pellets. The edge jump discontinuities were in the 0.2–0.8 range for all the edges/samples. Incident (I_o) and transmitted (I_1) X-ray intensities were measured by two ionization chambers opportunely filled with gas mixtures. After the I_1 chamber a metal foil was placed and used for energy calibration measuring the transmitted X-ray intensity (I_2) with a third ionization chamber. The $\alpha = \mu t$ absorption signals were calculated for samples ($\alpha_s = \ln(I_o/I_1)$) and references ($\alpha_r = \ln(I_1/I_2)$). In order to improve the data statistics and avoid artefacts due to X-ray beam drifts or instabilities at least three spectra were recorder for each sample and averaged up after checking for energy calibration which resulted very stable, within ±0.1 eV (Co and Ni K edges) or ±0.2 eV (Ag K edge). The signal to noise ratio was estimated better than some 10^3 in the experimental k-range. Repeated XANES spectra were compared in order to exclude radiation damage effects.

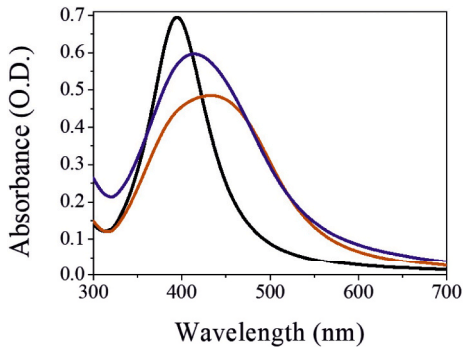

Fig. 1. Absorption spectra of AgNPs in presence of Co. The black line represents the reference (pure AgNPs solution), while the red and blue curves represent the optical behaviour of the solution with 1 and 5 ppm of Co^{2+} ions, respectively. (For interpretation of the references to colour in this figure legend, the reader is referred to the Web version of this article.)

The raw XAS spectra $\alpha(E)$ were treated with ESTRA program [15] following the standard procedures for linear pre-edge subtraction, post edge normalization and extraction of the experimental signal $\chi^{exp}(k)$. The edge energy E_o being the origin of photoelectron wavevector $k = \hbar^{-1}\sqrt{2m_e(E-E_o)}$ (m_e is electron mass), was selected at the first inflection point of the absorption signal and refined during the data analysis (see below).

The quantitative data analysis has been carried out using the FITEXA program [15] through a not linear least-square data refinement procedure in the reciprocal space k, minimizing the k^2-weighted sum of square differences: $\Delta^2 = \sum_j (k_j^2\chi^{exp}(k_j) - k_j^2\chi^{th}(k_j))^2$. The theoretical model curves χ^{th} were calculated as a sum of partial contributions using the standard EXAFS formula [16] for Gaussian shaped neighbour shell distribution. Each shell is characterized by the average coordination distance (R_i), the multiplicity number (N_i) and the variance (mean-square relative displacement, MSRD) σ^2. The theoretical amplitude, phase and mean free path functions required for the standard EXAFS formula were calculated using the FEFF 8.2 program [17], for atomic clusters built from crystallographic models.

High resolution X-ray Photoelectron Spectroscopy (HR-XPS) measurements were performed at the Elettra synchrotron radiation source (Trieste, Italy), using the Materials Science Beamline (MSB), that is positioned at the left end of the bending magnet 6.1. MSB is equipped with a plane grating monochromator providing SR light in the 21–1000 eV energy range. The UHV end station is equipped with a SPECS PHOIBOS 150 hemispherical electron analyser, low-energy electron diffraction optics, a dual-anode Mg/Al X-ray source, an ion gun, a sample manipulator with a K-type thermocouple attached to the rear side of the sample. For the here presented experiments we detected photoelectrons emitted by C1s, O1s, S2p, Ag3d core levels, using a normal emission geometry. In order to maximize signals intensity, we selected a photon energy value of 630 eV (impinging at 60° respect to the sample surface) for all elements except S; in order to maximize the intensity of S2p signals, that was expected to be very low due to element dilution, the S2p core level was measured with photon energy = 350 eV. Charging correction of binding energies (BEs) was done using as a reference the aliphatic C 1s (BE 285.0 eV). To fit core level spectra, we subtracted a Shirley background and then used Gaussian peak functions as signals components.

4. Data analysis results

4.1. Ni K-edge XAFS data analysis and results

The energy position of the X-ray absorption edge is directly related to the average valence state of the absorber [18]. Comparing the experimental Ni K-edge XANES measured on the Ni-1 ppm and Ni-5 ppm samples with the spectra measured on Ni metal foil (Ni^0) and NiO (Ni^{2+}) reference compounds (Fig. 2) it is possible to establish the Ni^{2+} valence

state in both the Ni loaded AgNPs samples.

The k^2-weighted EXAFS signal and the corresponding moduli of Fourier Transform (FT) measured on Ni-1 ppm and Ni-5 ppm samples are reported in Fig. 1 (S.I.). The spectra and the FT of both the samples are very similar, pointing out the same local structure around Ni, except the Ni-1ppm-AgNP spectral features appear slightly more attenuated suggesting more structural disorder. The Ni FTs show three main peaks at around 1.7 Å, 2.8 Å and 5.7 Å pointing out the positions (uncorrected for the photoelectron scattering phase shift) of main coordination shells around the average Ni absorber.

Comparing the Ni FT's with literature data [20,21] it is evident the close similarity with the FT's of Ni hydroxide ($Ni(OH)_2$) which is a compound made of layers of face sharing NiO_6 octahedra (Fig. 2), kept together by Van del Waals forces. To achieve quantitative structural details about the Ni local structure the raw k^2-weighted spectra were fitted in the 3–14 Å $^{-1}$ k-range. The model χ^{th} function is calculated as a sum of partial contribution assuming as a model the $Ni(OH)_2$ structure [22]. The two main FT peaks are assigned to the 6 oxygens directly bonded to Ni at around 2 Å from the absorber (Ni-O_1) and to the 6 Ni neigbhours in the Ni plane located around 3.13 Å from the absorber (Ni-Ni_2). The weak peak around 5.7 Å is likely associated to the Ni-Ni_2 and Ni-Ni_3 shells, noticeably the Ni-Ni_3 shell must include the multiple scattering (MS) contributions enhanced by the focusing effect of Ni-Ni_1-Ni_3 aligned configurations. The fit was improved adding the MS contribution Ni-O_2 at around 4 Å.

The contributions of other intermediate Ni-O shells were not considered in the analysis as preliminary tests demonstrate they have statistically not significant contribution to the best fit, such a weak signal is likely due to the combined effect of disorder and weakness of the oxygen scattering factors. The structural signal from the inter-layer coordination was also found negligible, likely due to the weakness of the Van del Waals forces between the layers giving rise to large structural disorder.

In order to reduce the number of free parameters in the fitting the multiplicity numbers of the shells involving N_i were constrained to the values in the $Ni(OH)_2$ model while the R_i and σ_1^2 were refined for each shell. It is expected that the experimental edge energy E_o, defined during the data treatment, differs from the theoretical one calculated by the FEFF program on the basis of the atomic potential models, therefore an energy shift ΔE_o was preliminary refined in the analysis and fixed the same for both Ni-1 ppm and Ni-5 ppm samples.

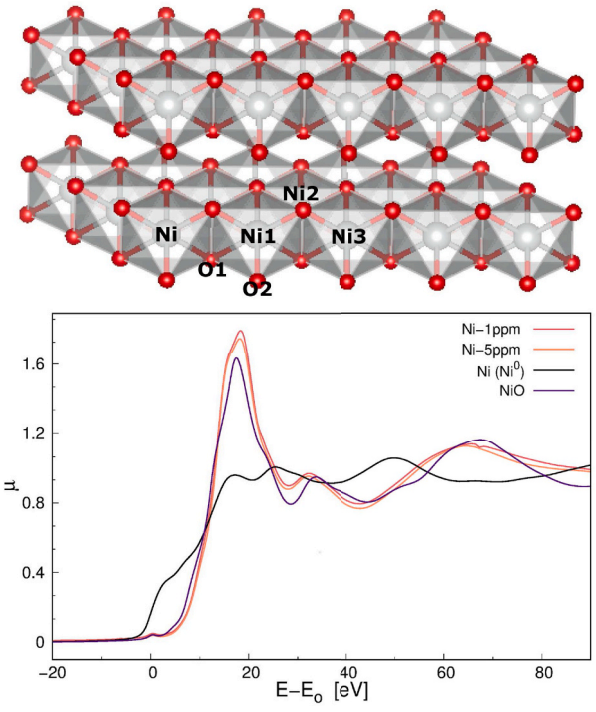

Fig. 2. Top: the $Ni(OH)_2$ layered structure [19]. Representative neighbours around a selected Ni absorber are shown, labelled as O_i and Ni_i for sake of clarity. Bottom: the XANES of Ag-Ni data are reported and compared with the Ni K edge spectra measured on Ni foil, NiO and $Ni(OH)_2$ reference samples.

This procedure allowed to achieve the best fit agreement and reproduces the main structural features till around 6 Å, the experimental spectra and best fit are reported in Fig. 3, the best fit agreement demonstrates the goodness of the structural model, the partial contributions used in the analysis and residuals for the Ni-1 ppm sample are shown as example. The best fit parameters resumed in Table 1 are in good agreement with the $Ni(OH)_2$ structure [21].

Comparing the local structure parameters of Ni-1 ppm and Ni-5 ppm samples it is evident the agreement with the $Ni(OH)_2$ structure. The nearest neighbour Ni-O_1 bond lengths appear the same in both samples, within the experimental uncertainty, while the Ni-Ni_1 and Ni-Ni_3 shells appear slightly contracted and more disordered in Ni-1 ppm sample respect to Ni-5 ppm as qualitatively suggested by the data in Fig. 1 (S.I.).

In both Ni-1 ppm and Ni-5 ppm spectra we cannot individuate some contribution that could be associated with a direct interaction between Ni and Ag.

4.2. Co K-edge XAFS data analysis and results

In order to asses the average Co oxidation state in our Co-loaded AgNPs, the experimental Co K-edge XANES measured on the Co-1 ppm and Co-5 ppm samples are compared with the XANES spectra measured on reference compounds (Fig. 4), namely Co metal foil (Co^0), CoO (Co^{2+}) and Co_3O_4 (1/3 Co^{2+} and 2/3 Co^{3+}). It is evident that the edge energy (E_{Co}) of Co-1 ppm and Co-5 ppm samples are higher than Co_3O_4 suggesting a higher Co oxidation state for Co load onto the AgNPs. In order to evaluate the average Co oxidation state in AgNPs loaded Co we used the integral method described in Ref. [23] to evaluate the E_{Co}.

From the CoO and Co_3O_4 spectra, in which Co has respectively 2+ and 2.66 + average oxidation state we obtained the energy shift of 2.35 (5) eV per charge unit, this allows to calculate an average Co oxidation state around 2.9(05) in both the samples, pointing out about 90% of Co in 3+ oxidation state.

The k^2-weighted EXAFS signal and the corresponding FT measured on Co-1 ppm and Co-5 ppm samples are reported in Fig. 2 (S.I.). The shape of Co K edge FTs are similar to those obtained from Ni data (Fig. 1 (S.I.)) with two main peaks at around 1.4 Å and 2.5 Å followed by weaker features around 5.5 Å suggesting also for the Co a layered structure such as Co-hydroxide or Co-oxy-hydroxide [25].

The two phases, Co-oxy-hydroxide and Co-hydroxide, have both a layered structure formed by octahedral sites where 6 oxygen atoms are symmetrically arranged around a central cobalt atom (see Fig. 4). The major difference between them is in the hydrogen bonds: in $Co(OH)_2$ each oxygen atom is bounded to a hydrogen atom at a distance of 0.95 Å, while in CoO(OH) the hydrogen atoms act as a bridge between two adjacent layer, it means that oxygen atoms of different layers are bounded to the same hydrogen at a distance of 1.26 Å [26]. The higher Co valence sate (3+) in CoO(OH) also has effect in the Co-O coordination distance that reflects in the next neighbour structure too as highlighted in Table 2. The interatomic distances of the two phases are reported in Table 2 The crystallographic structure of Co-oxy-hydroxide has contracted bond lengths with respect to Co-hydroxide [see Table 2], so it is in a better agreement with our experimental results.

The k^2-weighted Co K-edge spectra were fitted in the k range 3–15 Å^{-1} applying the same procedure described for the Ni samples and assuming a Co-oxy-hydroxide layered structure. The two main FT peaks are assigned, as for Ni, to the 6 oxygen directly bonded to Co around 1.9 Å from the absorber (Co-O_1) and to the 6 Co neigbhours in the Co plane

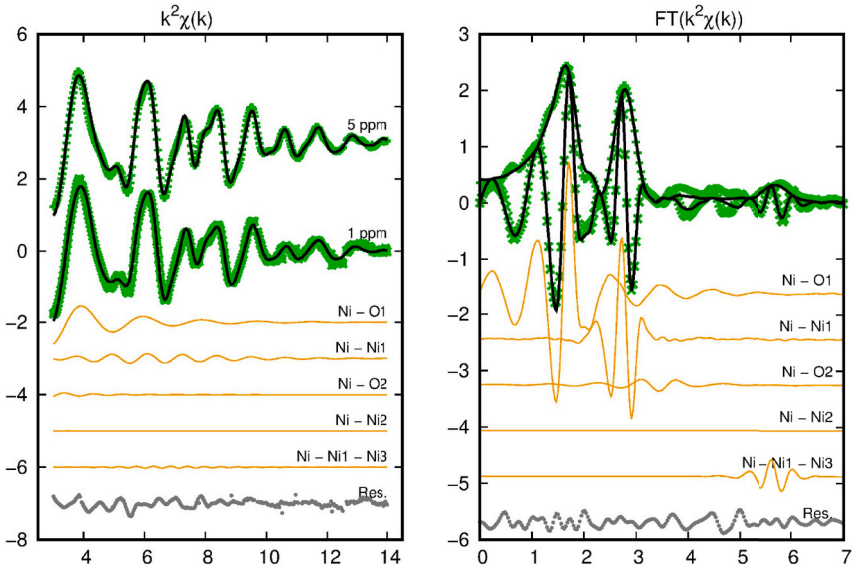

Fig. 3. The figure shows the results of the best fit for Ni K edge EXAFS data. Left: Data (green dots) and best fit line (black line) in k-space for both the NP samples (vertically shifted). The partial contributions used in the structural model and the residual are shown for Ni-1 ppm sample, vertically shifted for sake of clarity. Right: Moduli of the Fourier transforms of experimental data (green dots) and best fit (black lines) for both the NP samples. The FT imaginary parts of experimental spectrum (green dots) and best fit (black line) are shown for the Ni-1 ppm sample. The FT imaginary parts of the partial contributions used fitting the Ni-1 ppm NP sample are shown, vertically shifted. The refinement demonstrates a good agreement till around 6 *Å* (uncorrected for the phase shift). (For interpretation of the references to colour in this figure legend, the reader is referred to the Web version of this article.)

Table 1
Best fit results for Ni K Edge XAFS Data Analysis. The structural data (interatomic distances and coordination numbers) of $Ni(OH)_2$ [19] have also been reported for sake of comparison.

Shell	Ni − O_1		Ni − Ni_1		Ni − O_2		Ni − Ni_2		Ni − Ni_1 −Ni_3	
Sample	R(Å)	σ^2(× 10^2 Å^2)	R(Å)	σ^2(× 10^2 Å^2)	R(Å)	σ^2(× 10^2 Å^2)	R(Å)	σ^2(× 10^2 Å^2)	R(Å)	σ^2(× 10^2 Å^2)
Ag-Ni 1 ppm	2.05(1)	0.65(3)	3.09(1)	0.82(4)	3.70(1)	0.22(1)	5.57(1)	0.52(1)	6.12(2)	0.94(5)
Ag-Ni 5 ppm	2.05(1)	0.72(4)	3.11(1)	0.66(3)	3.68(1)	0.24(1)	5.11(1)	0.19(3)	6.16(2)	0.60(3)
	R(Å)	N	R(Å)	N	R(Å)	N	R(Å)	N	R(Å)	N
$Ni(OH)_2$	2.08	6	3.12	6	3.75	12	5.40	6	6.24	6

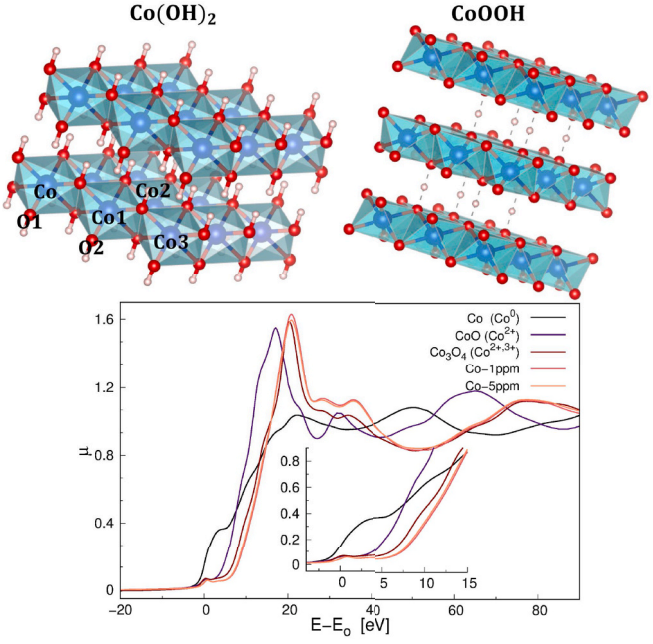

Fig. 4. Top: Co-hydroxide [24] and Co-oxy-hydroxide [25] structure: the two phases have the same layered structure but they differ in the hydrogen bonds. Representative neighbours around a selected Co absorber are shown, labelled as O_i and Ni_i for sake of clarity. Bottom: the XANES of Ag-Co data are reported and compared with Co K edge spectra measured on Co foil, CoO and Co_3O_4 reference samples.

around 2.8 Å from the absorber (Co-Co_2). As for the Ni data we improved the fitting adding the MS contribution Co-Co_1-Co_3 at around 5.7 Å while the contributions from far away Co-O and interlayer coordinations were neglected. We included here the Co-O_2 (around 3.4 Å) and the Co-Co_2 (around 4.9 Å) shells as we found statistically significant the best fit improvement. The edge energy shift (ΔE_o) was refined as for the Ni data.

The experimental spectra and best fit are reported in Fig. 5 together with the partial contributions used in the analysis and residuals for the Co-1 ppm sample. The structural parameters resulting from the analysis are reported in Table 2. The good best fit agreement supports the Co-oxy-hydroxide layered model, similarly to what observed for Ni loaded AgNP samples. The Co local structure appears compressed respect to Ni one, with the Co-O_1 shell found at 1.9 Å and the Co-Co_2 at 2.85 Å. Accordingly to the Ni structure the Co-1 ppm local structure appears more disordered (larger σ^2) respect to Co-5 ppm sample. We tried to recognize in the EXAFS region some contribution from the Co (2+) phases, as suggested by the XANES analysis but these attempts did not improve the best fit quality, nor in the Table 2 we can individuate some specific effect coming from Co^{2+} phases. Such apparent discrepancy between XANES and EXAFS analysis is not surprising because the absorption signal in the XANES region is very sensitive to the contributions coming from the absorber in phases with different valence states and/or local coordination chemistry [18]. Such a sensitivity is definitively weaker in the EXAFS region due to structural disorder dampening the details from diluted phases and from the weaker coordination shells. As for Ni XAFS results, in both Co-1 ppm and Co-5 ppm spectra we cannot individuate some contribution that could be associated with a direct interaction between Co and Ag.

Table 2
Best fit results for Co K Edge XAFS Data Analysis. The structural data (interatomic distances and coordination numbers) of Co-hydroxide $Co(OH)_2$ [24] and Co-oxy-hydroxide CoO(OH) [27] have also been reported for sake of comparison, the better agreement of the experimental data with the CoO(OH) structure is clearly evident.

Shell	Co − O_1		Co − Co1		Co − O_2		Co − Co_2		Co − Co_1 −Co_3	
Sample	R(Å)	$\sigma^2(\times 10^2$ Å$^2)$	R(Å)	$\sigma^2(\times 10^2$ Å$^2)$	R(Å)	$\sigma^2(\times 10^2$ Å$^2)$	R(Å)	$\sigma^2(\times 10^2$ Å$^2)$	R(Å)	$\sigma^2 \cdot 10^{-2}$(Å^2)
Ag-Co 1 ppm	1.90(1)	0.33(2)	2.85(1)	0.54(3)	3.38(1)	0.44(2)	4.97(1)	0.59(3)	5.78(1)	0.50(3)
Ag-Co 5 ppm	1.90(1)	0.184(9)	2.85(1)	0.39(2)	3.37(1)	0.14(1)	4.97(1)	0.34(2)	5.77(1)	0.37(2)
	R(Å)	N	R(Å)	N	R(Å)	N	R(Å)	N	R(Å)	N
$Co(OH)_2$	2.12	6	3.19	6	3.82	12	5.52	6	6.37	6
CoO(OH)	1.90	6	2.86	6	3.43	12	4.95	6	5.71	6

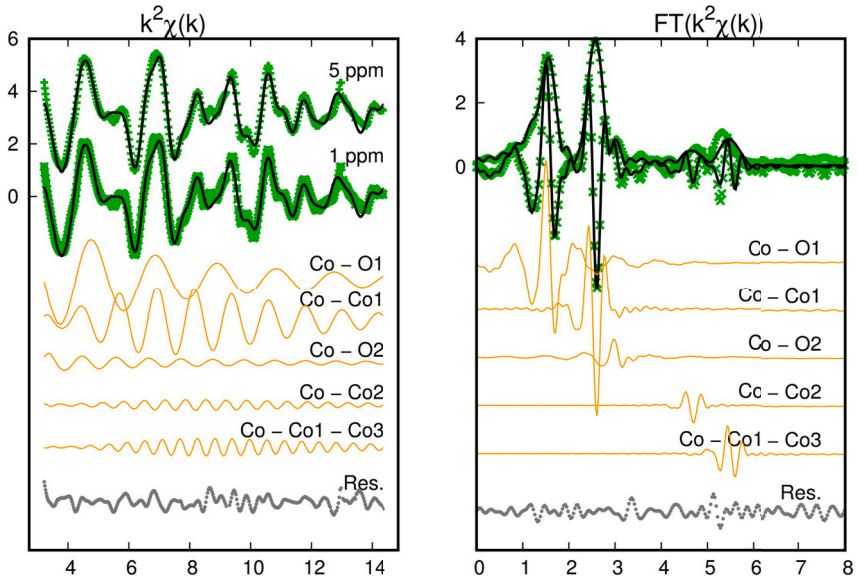

Fig. 5. The figure shows the results of the best fit for Co K edge EXAFS data. Left: Data (green dots) and best fit line (black line) in k-space for both the NP samples (vertically shifted). The partial contributions used in the structural model and the residual are shown for sample 1 ppm, vertically shifted for sake of clarity. Right: Moduli of the Fourier transforms of experimental data (green dots) and best fit (black lines) for both the NP samples. The FT imaginary parts of experimental spectrum (green dots) and best fit (black line) are shown for sample 1 ppm. The FT imaginary parts of the partial contributions used fitting the NP sample 1 ppm are shown, vertically shifted. The refinement demonstrates a good agreement till around 6 Å. (For interpretation of the references to colour in this figure legend, the reader is referred to the Web version of this article.)

4.3. XPS data analysis

HR-XPS measurements were performed on AgNPs-3MPS treated with 5 ppm ions solutions with the aim to assess the silver nanoparticles molecular stability and integrity; in addition, Ni2p and Co2p XPS spectra provided information about the heavy metal ions oxidation states supporting XAS analysis results. HR-XPS data collected at the C1s, O1s, S2p and Ag3d core levels confirm the molecular structure and stability of AgNPs-3MPS, as already extensively discussed in Ref. [11, 28]; a complete collection of HR-XPS data (Binding Energy – BE – values, full width half maxima – FWHM - and assignments) are collected in Table I in the Supporting Information. Co2p and Ni2p HR-XPS spectra are reported in Fig. 6a and b respectively; data analysis results are summarized in Table 3.

For Ni2p signal, a single spin-orbit pair is observed, with the expected satellite structure (see Fig. 6b); the Ni2p BE position is indicative for Ni^{2+} ions as suggested by the literature [15,29] and in agreement with the XANES results.

Looking at the Co2p XPS spectrum it appears composite, and by applying a peak fitting procedure it is possible to individuate at least three contribution to the main signal; the two Gaussian curves at lower BE (779.89 eV; 781.37 eV) are consistent with $Co2p_{3/2}$ components of Co^{3+} and Co^{2+} signals assigned in the literature to respectively CoO(OH) and $Co(OH)_2$ species [17,20,21], as also confirmed by the satellite structures (magenta and violet peaks in Fig. 6a) and accordingly with XAS data analysis findings. The spin-orbit pair at higher BE (783.06 eV) is likely due to cobalt chlorine impurities [30] arising by the synthesis procedure. The Co^{3+}:Co^{2+} peak area ratio is 1.9:1, this finding is apparently at conflict with the results obtained from XANES but, owing

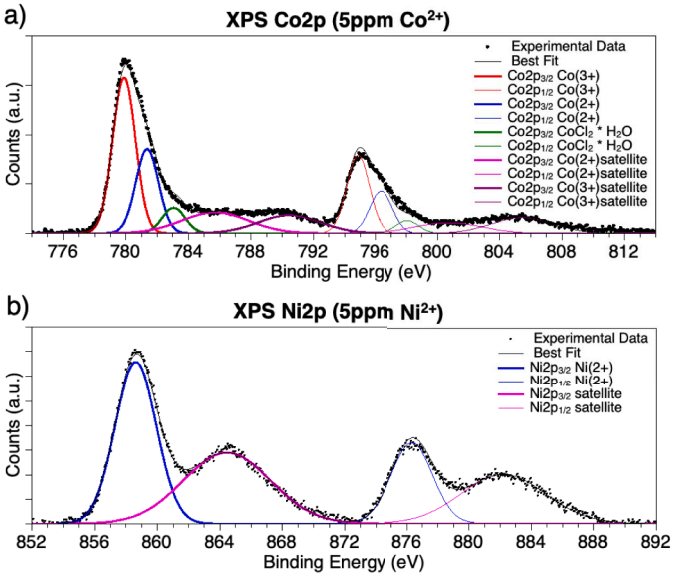

Fig. 6. Co2p (a) and Ni2p (b) XPS spectra collected on AgNPs-3MPS treated with heavy metal ions solutions at 5 ppm concentration.

the XPS sensitivity to the close surface regions (sampling depth for XPS analysis with the experimental set-up used for this experiment is about 5 nm [31]), this contrast brings interesting information. Combining XPS (surface) and XAFS (bulk) information it appears that Co loading on

Table 3
Co2p and Ni2p signals positions (BE), FWHM, Atomic ratios, theoretical Atomic Ratios and Assignments for the two samples treated with 5 ppm heavy metal ion solutions.

Signal	BE (eV)	FWHM (eV)	Assignment
$Co2p_{3/2}$	779.89	1.71	CoO(OH) - Co(III)
	781.37	1.71	Co(OH)2 - Co(II)
	783.06	1.71	CoCl2 * H2O
	785.71	5.00	Co(II) satellite
	790.49	4.36	Co(III) satellite
$Ni2p_{3/2}$	856.86	3.12	Ni(II)
	862.24	6.58	Ni(II) satellite

AgNPs gives rise to a more complex morphology of AgNPs-Metal aggregates with an inner region richer in CoO(OH), representing about 90% of the total Co content, while the $Co(OH)_2$ dominates in the region close to the surface.

4.4. Ag K edge XAFS and results

The k^2-weighted Ag K-edge EXAFS signal measured for Ni and Co samples are shown in Fig. 3 (S.I.) together with their k^2-weighted FTs. The Ag data appear all very similar, suggesting that there are no significant structural changes in the NP cores. The analysis was carried out along the way described in Refs. [32] in order to get information about the Ag local structure at the NP surface. The proposed model assumes two different Ag phases: an Ag fcc phase (labelled as Ag^{bulk})) representing the NP core, and an Acantite-like (Ag_2S) [32] phase representing the contribution of Ag ions at the NP surface. The model includes single and relevant multiple scattering therms, constrained to the crystallographic models. Due to the large number of parameters involved, crystallographic constraints were applied to the coordination distances as described in Ref. [32] in order to reduce the correlation effects. The coordination numbers are constrained in order to take into account the fraction of Ag in fcc and Ag_2S phases. The best fit are presented in Fig. 7 for the three samples, the partial contributions associated to the Ag-phase (NP core) and Ag_2S-like phase (NP surface shell) are shown for 1 ppm sample as example, the best fit parameters are resumed in Table 4.

5. Conclusions

The average electronic state, coordination chemistry and local atomic structure of Co and Ni ions adsorbed onto AgNPs have been studied combining XAFS and XPS analysis.

The analysis of the XANES regions of Ni and Co has provided information about the average valence state of adsorbed metals [18]. The near edge region (XANES) of the normalized spectra for Co and Ni are presented in Figs. 2 and 4, for each metal both 1-ppm and 5-pmm spectra have the very same shape and appear well aligned in energy, meaning that the average local atomic structure and average electronic state of the absorbers are not affected by concentration.

The analysis of the Ag K edge point out a Ag metal-core/Ag_2S-shell nature of the NP, the core diameter being 6–8 nm region. The analysis of Co and Ni K edge XAFS spectra demonstrates that both the metals appear in form of hydroxides with some difference between Ni and Co. In particular the Ni-K edge energy position is in good agreement with Ni^{2+} valence state and the EXAFS analysis demonstrate a Ni-hydroxide, $Ni(OH)_2$, phase in both the samples. The Co-K edge XANES of Co samples show that most of the Co (more than 90%) is in Co^{3+} oxidation state, the EXAFS analysis allowed to recognize the Co-oxyhydroxide, CoO(OH) local structure. This finding, compared with the XPS results, suggests the Co^{3+} mainly located in the bulk of Co-AgNPs aggregates, while reduced Co^{2+} ions mainly reside close to the surface.

It is significant to note that there is no evidence from the XAFS (Ag, Co or Ni K edge data) of any Ag-M (M = Co, Ni) coordination, pointing out the absence of a direct interaction between the NP core and the 3d metals. This is a relevant finding, in excellent agreement with our previous studies [11,13] which hypothesised the formation of coordination compounds of Co/Ni. Indeed the 3MPS stabilized AgNPs were considered able to coordinate the positively charged metal ions thanks to the negatively charged sulfonate moiety of 3MPS, inducing the formation of AgNPs aggregates catching Co or Ni [11,13]. Here the direct evidence metal hydroxides such as $Ni(OH)_2$ and CoO(OH) demonstrates the metal

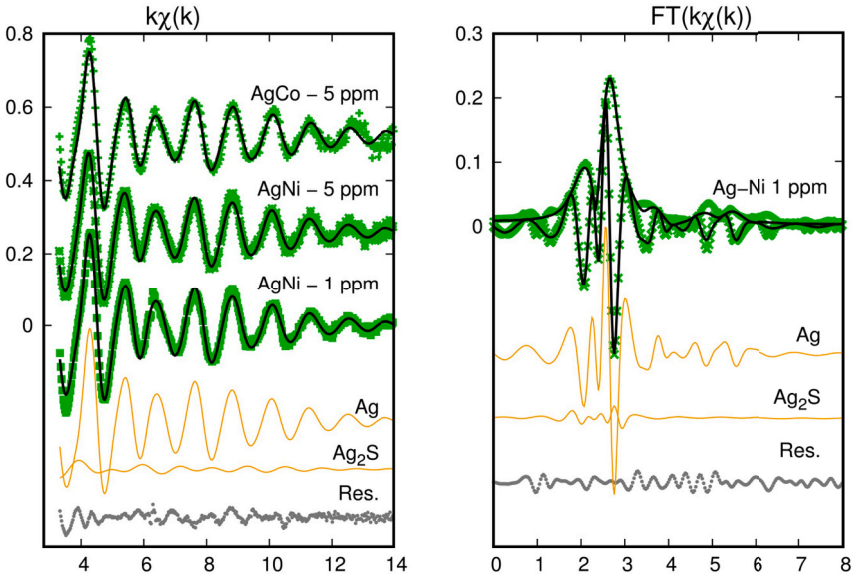

Fig. 7. The figure shows the result of the analysis of Ag K edge data. In the top left figure the experimental (green) and best fit (black line) are represented in k space for all the sample investigated, shifted vertically for sake of clarity. The two panels on the right reports an example of fit for the Ag - Ni 1 ppm sample. The upper panel shows the Fourier transform (FT) modulus and imaginary part of experimental $k\chi(k)$ (green dots) and theoretical $k\chi(k)$ (black lines). The FT imaginary parts of Ag and Ag_2S contributions are also shown (yellow lines vertically shifted). The residual is also shown for sake of completeness. The lower panel shows the same fit in k space. (For interpretation of the references to colour in this figure legend, the reader is referred to the Web version of this article.)

Table 4
Best fit results for Ag K Edge XAFS Data Analysis.

	Phase	Ag^M		Ag_2S			
Sample	Shell	$R_{AgAg(Å)}$	$\sigma^2_{AgAg}(\times 10^2 Å^2)$	$R_{AgS(Å)}$	$\sigma^2_{AgS}(\times 10^2 Å^2)$	$R_{AgAg(Å)}$	$\sigma^2_{AgAg}(\times 10^2 Å^2)$
Ag-Co 5 ppm		2.85(1)	0.84(4)	2.48(1)	0.62(3)	3.04(1)	0.60(3)
Ag-Ni 5 ppm		2.85(1)	0.90(5)	2.50(1)	0.81(4)	3.04(1)	1.11(5)
Ag-Ni 1 ppm		2.85(1)	0.95(5)	2.43(1)	0.53(3)	3.04(1)	0.67(3)

ions does not react with 3MPS-AgNPs as isolated ions, but the presence of hydroxides being reactive species, provides an additional mechanism leading to the formation of AgNPs aggregates catching metal contaminants.

Declaration of competing interest

The authors report no conflicts of interest in this work.

CRediT authorship contribution statement

Irene Schiesaro: Investigation, Formal analysis, Writing - original draft, Writing - review & editing. **Chiara Battocchio:** Conceptualization, Investigation, Formal analysis, Writing - review & editing. **Iole Venditti:** Resources, Writing - review & editing. **Paolo Prosposito:** Resources, Writing - review & editing. **Luca Burratti:** Resources, Writing - review & editing. **Paolo Centomo:** Writing - review & editing. **Carlo Meneghini:** Conceptualization, Investigation, Formal analysis, Supervision, Writing - review & editing.

Acknowledgements

The Grant of Excellence Departments, MIUR (ARTICOLO 1, COMMI 314–337 LEGGE 232/2016), is gratefully acknowledged by authors of Roma Tre University. This research was partially funded by Regione Lazio, through Progetto di ricerca 85-2017-15125, according to L.R.13/08. We gratefully acknowledge the assistance of our colleagues at Elettra for providing good quality synchrotron light. CERIC-ERIC consortium, Grant Agency of Charles University (GAUK project No. 1054217) and Czech Ministry of Education (LM2015057) are acknowledged for the access to experimental facility and financial support.

Appendix A. Supplementary data

Supplementary data to this article can be found online at https://doi.org/10.1016/j.physe.2020.114162.

References

[1] L. Jarup, Impact of environmental pollution on health: balancing risk, Br. Med. Bull. 68 (2003) 167–182.
[2] V. Rajaganapathy, F. Xavier, D. Sreekumar, P. Mandal, Heavy metal contamination in soil, water and fodder and their presence in livestock and products: a review, J. Environ. Sci. Technol. 4 (3) (2011) 34–249.
[3] J. Duruibe, M. Ogwuegbu, J. Egwurugwu, Heavy metal pollution and human biotoxic effects, Int. J. Phys. Sci. 2 (5) (2007) 112–118.
[4] World health organization, Guidelines for Drinking-Water Quality: Fourth Edition Incorporating the First Addendum, *World Health Organization*, Geneva, Switzerland, 2017.
[5] H.N. Kim, W.X. Ren, J.S. Kim, J. Yoon, Fluorescent and colorimetric sensors for detection of lead, cadmium, and mercury ions, Chem. Soc. Rev. 41 (2012) 3210–3244.
[6] A.-J. Wang, H. Guo, M. Zhang, D.-L. Zhou, R.Z. Wang, J.-J. Feng, Sensitive and selective colorimetric detection of cadmium(ii) using gold nanoparticles modified with 4-amino-3-hydrazino-5-mercapto-1,2,4-triazole, Microchim. Acta 180 (2013) 1051–1057.
[7] J. Yin, T. Wu, J. Song, Q. Zhang, S. Liu, R. Xu, H. Duan, Sers-active nanoparticles for sensitive and selective detection of cadmium ion (cd2+), Chem. Mater. 23 (21) (2011) 4756–4764.
[8] M. Zhang, Y.-Q. Liu, B.-C. Ye, Colorimetric assay for parallel detection of cd2+, ni2+ and co2+ using peptide-modified gold nanoparticles, Analyst 137 (2012) 601–607.
[9] B.A. Makwana, D.J. Vyas, K.D. Bhatt, S. Darji, V.K. Jain, Novel fluorescent silver nanoparticles: sensitive and selective turn off sensor for cadmium ions, Appl. Nanosci. 6 (2016) 555–566.
[10] A. Moores, F. Goettmann, The plasmon band in noble metal nanoparticles: an introduction to theory and applications, New J. Chem. 30 (2006) 1121–1132.
[11] F. Mochi, L. Burratti, I. Fratoddi, I. Venditti, C. Battocchio, L. Carlini, G. Iucci, M. Casalboni, F.D. Matteis, S. Casciardi, S. Nappini, I. Pis, P. Prosposito, Plasmonic sensor based on interaction between silver nanoparticles and Ni^{2+} or Co^{2+} in water, Nanomaterials 8 (7) (2018) 488.
[12] P. Prosposito, F. Mochi, E. Ciotta, M. Casalboni, F.D. Matteis, I. Venditti, L. Fontana, G. Testa, I. Fratoddi, Hydrophilic silver nanoparticles with tunable optical properties: application for the detection of heavy metals in water, Beilstein J. Nanotechnol. 7 (2016) 1654–1661.
[13] P. Corsi, I. Venditti, C. Battocchio, C. Meneghini, F. Bruni, P. Prosposito, F. Mochi, B. Capone, Designing an optimal ion adsorber at the nanoscale: the unusual nucleation of AgNP/Co^{2+}–Ni^{2+}binary mixtures, J. Phys. Chem. C 123 (6) (2019) 3855–3860.
[14] A.D. Cicco, G. Aquilanti, M. Minicucci, E. Principi, N. Novello, A. Cognigni, L. Olivi, Novel xafs capabilities at elettra synchrotron light source, J. Phys. Conf. Ser. 190 (2009) no. 012043.
[15] C. Meneghini, F. Bardelli, S. Mobilio, Estra-fitexa: a software package for exafs data analysis, Nucl. Instrum. Methods Phys. Res. B 285 (2012) 153–157.
[16] J.J. Rehr, R.C. Albers, Theoretical approaches to x-ray absorption fine structure, Rev. Mod. Phys. 72 (2000) 621.
[17] A.L. Ankudinov, B. Ravel, J. Rehr, S.D. Conradson, Real-space multiple-scattering calculation and interpretation of x-ray-absorption near-edge structure, Phys. Rev. B 58 (1998) 7565.
[18] M. Benfatto, C. Meneghini, A close look into the low energy region of the XAS spectra: the XANES region. Plus 0.5em minus 0.4emIn, in: S. Mobilio, F. Boscherini, C. Meneghini (Eds.), Synchrotron Radiation, Springer, Berlin, Heidelberg, 2015.
[19] C.S.T.N. Ramesh, P.V. Kamath, Classification of stacking faults and their stepwise elimination during the disorder-order transformation of nickel hydroxide, Acta Crystallogr. Sec. B 62 (2006) 530–536.
[20] Y. Ichiyanagi, H. Kondoh, T. Yokoyama, K. Okamoto, K. Nagai, T. Ohta, X-ray absorption fine-structure study on the $Ni(OH)_2$ monolayer nanoclusters, Chem. Phys. Lett. 379 (2003) 345–350.
[21] Y. Zhu, C. Cao, S. Tao, W. Chu, Z. Wu, Y. Li, Ultrathin nickel hydroxide and oxide nanosheets: synthesis, characterizations and excellent supercapacitor performances, Sci. Rep. 4 (2015) 5787.
[22] R.W. Cairns, E. Ott, X-ray studies of the system nickel-oxygen-water. i. nickelous oxide and hydroxide, J. Am. Chem. Soc. 2 (55) (1993) 527–533.
[23] H. Dau, P. Liebisch, M. Haumann, X-ray absorption spectroscopy to analyze nuclear geometry and electronic structure of biological metal centers—potential and questions examined with special focus on the tetra-nuclear manganese complex of oxygenic photosynthesis, Anal. Bioanal. Chem. 376 (2003) 562–583.
[24] H.K.Q. Zhao, Where does the density localize in the solid state? divergent behavior for hybrids and dft+u, J. Chem. Theor. Comput. 14 (2) (2018) 670–683.
[25] M. Risch, F. Ringleb, M. Kohlhoff, P. Bogdanoff, P. Chernev, Z. Ivelina, D. Holger, Water oxidation by amorphous cobalt-based oxides: in situ tracking of redox transitions and mode of catalysis, Energy Environ. Sci. 8 (2015) 661–674.
[26] D. Upadhyaya, B. Roondheb, A. Pratapa, P.K. Jhab, Two-dimensional Delafossite Cobalt Oxyhydroxide as a Toxic Gas, vol. 476, 2019.
[27] H.G.M. Deliens, Polytypism of heterogenite, Mineral. Mag. 39 (1973) 152–157.
[28] P. Prosposito, L. Burratti, A. Bellingeri, G. Protano, C. Faleri, I. Corsi, C. Battocchio, G. Iucci, L. Tortora, V. Secchi, S. Franchi, I. Venditti, Bifunctionalized silver nanoparticles as Hg^{2+} plasmonic sensor in water: synthesis, characterizations, and ecosafety, Nanomaterials 9 (10) (2019) 1353.
[29] S.C. Petitto, M.A. Langell, Surface composition and structure of Co_3O_4(110) and the effect of impurity segregation, J. Vac. Sci. Technol. 22 (2004) 1960.
[30] L.J. Matienzo, L.I. Yin, S.O. Grim, W.E. Swartz, X-ray photoelectron spectroscopy of nickel compounds, Anal. Chem. 12 (12) (1973) 2762–2769.
[31] P. Swift, D. Shuttleworth, M.P. Seah, in: D. Briggs, M.P. Seah (Eds.), Practical Surface Analysis by Auger and X-Ray Photoelectron Spectroscopy, J. Wiley & Sons, Chichester, 1983 chapter 4.
[32] C. Battocchio, C. Meneghini, I. Fratoddi, I. Venditti, M.V. Russo, G. Aquilanti, C. Maurizio, F. Bondino, R. Matassa, M. Rossi, S. Mobilio, G. Polzonetti, Silver nanoparticles stabilized with thiols: a close look at the local chemistry and chemical structure, J. Phys. Chem. C 116 (36) (2012) 19571–19578.